JOURNAL OF MATERIALS SCIENCE 27 (1992) 5365–5374

Dislocation configurations and internal stresses in the creep of Nimonic 91

C. K. L. DAVIES, A. G. OLDER*, R. N. STEVENS
Department of Materials, Queen Mary and Westfield College, Mile End Road, London E1 4NS, UK

The internal stress, σ_i, developed during the creep of Nimonic 91 was determined as a function of applied stress, σ_a, using the strain transient dip technique. Transmission electron microscope observations of thin films of crept specimens showed Orowan dislocation loops to exist around γ' phase particles at low stresses with partial dislocation loops around faulted γ' particles at high stresses. The numbers of loops per specimen volume were counted and the resulting internal stress calculated. The results indicate that a significant part of the mechanically measured internal stress can be attributed to Orowan loops around γ' particles which are stabilized against climb by the superlattice fault resulting from partial penetration of the γ' particle by the dislocation. The variation of internal stress with applied stress can be accounted for qualitatively by the variation of loop density with stress at low stresses and the initiation of relaxation processes involving partial or complete shearing of γ' particles by loops at high stresses. It is suggested that creep in Nimonic 91 is dependent on the magnitude of the effective $(\sigma_a - \sigma_i)$ and that the internal stress is determined largely by the density of dislocation loops around γ' particles.

1. Introduction

It has long been recognized that internal stresses are developed during deformation of materials and that these internal stresses play an important role in determining mechanical properties. At any point in the material after deformation there is a local effective stress which is the sum of the stress due to the externally applied forces and the local internal stress. The mechanics and kinetics of the deformation processes occurring in these local regions are determined by, amongst other things, the local effective stress. The mechanical behaviour of the material body as a whole is some sort of total or average of the behaviour of all its regions. How this sum is accomplished by the material body is by no means simple and may be dislocation mechanism specific. Nevertheless after the passage from the microscopic regions to the macroscopic material body it is still possible to discern an effective stress which is different from the applied stress. At this macroscopic level the applied stress is σ_a and the internal stress is $-\sigma_i$, where the convention of a negative sign is used to make the internal stress, which is opposite in sign to the applied stress, into a positive quantity. The macroscopic effective stress σ_e is thus given by

$$\sigma_e = \sigma_a - \sigma_i \quad (1)$$

It is generally believed that internal stresses play an important role in the creep of alloys hardened by a dispersion of strong, relatively undeformable precipitates. Such materials often exhibit a stress sensitivity of the creep rate which is far too high to be explained if the deformation events and the rate-controlling processes are determined by the applied stress alone [1–9]. If there is a high internal stress which is relatively constant and opposes the applied stress, however, a small change in applied stress gives rise to a large relative change in the effective stress resulting in a large change in creep rate and an apparently high stress sensitivity.

Measurements of the macroscopic internal stress have been carried out using the technique given the name "strain transient dip test" [10] and also a technique involving the observation of the effect of cumulative small stress reductions on the creep rate [11]. It should be noted, however, that the originators of the latter method did not claim that it measured an internal stress and there is no apparent reason why both methods should yield the same result. Furthermore, results from the strain transient dip test should be treated with caution and examined in light of the dislocation configurations yielding the internal stress and of the rate-controlling creep mechanisms. Attempts to identify the dislocation configurations which give rise to the internal stress have been largely speculative and it has not been possible to make meaningful comparisons of the internal stresses determined from mechanical measurements with those calculated from observations of particular dislocation configurations.

* *Present address*: HW Computer Services, Phoenix House, Christopher Martin Road, Basildon, Essex, UK.

0022–2461

The present paper reports mechanical measurements of internal stresses developed during the creep of a nickel-based γ' precipitate hardened alloy, Nimonic 91, together with calculations of the internal stress resulting from observations of the dislocation configurations developed during creep. In this alloy, given the appropriate heat treatment, Orowan dislocation loops are the main contributors to the internal stress. It is this relatively simple dislocation configuration which enables an unambiguous calculation to be made of the internal stress, allowing, for the first time, a comparison to be made with the internal stress resulting from mechanical measurement.

2. Internal stresses resulting from Orowan loops

Internal stresses, often called residual stresses by engineers, are zero, or at least small initially in an undeformed specimen. They increase with strain and vary from point to point in a deforming specimen. Internal stresses arise when plastic deformation is heterogeneous, that is when some regions of the specimen experience more plastic deformation than others, which in turn have a comparatively larger component of elastic deformation. There are therefore always regions in the specimen where the internal stress is in the same sense as the applied stress as well as regions where it opposes the applied stress. Hence if every volume element were sampled with equal probability by dislocations the internal stress would average zero.

If, on the other hand, dislocations are unable to sample the regions of negative (note the sign convention) internal stress (high effective stress) and only sample regions of positive internal stress (low effective stress) then the average internal stress would be finite and negative, so as to oppose the applied stress. This is the case if precipitate particles are not sheared by dislocations but by-passed by Orowan looping [12, 13].

The internal stresses associated with Orowan loops can be understood by considering the following series of processes illustrated by Fig. 1a–d. The particle and matrix are initially unstrained and the particle is then imagined to be removed from the matrix as in Fig. 1a. The matrix is then deformed plastically, which is represented by the passage of a single dislocation leaving a slip step on the surface of the hole (Fig. 1b). The particle must now be re-fitted back into the hole. To do this, forces are applied to both the surface of the hole and to the surface of the particle until they are both the same shape and until the forces at corresponding points are equal and opposite, as in Fig. 1c. It can be seen that these forces develop stresses inside the particle which are in the same sense as the applied stress which caused the plastic shear of the matrix, while stresses of the opposite sense are produced in the matrix itself. The particle can now be placed back in position in the matrix. The average internal stresses in both particle and matrix will be zero, but if the particle

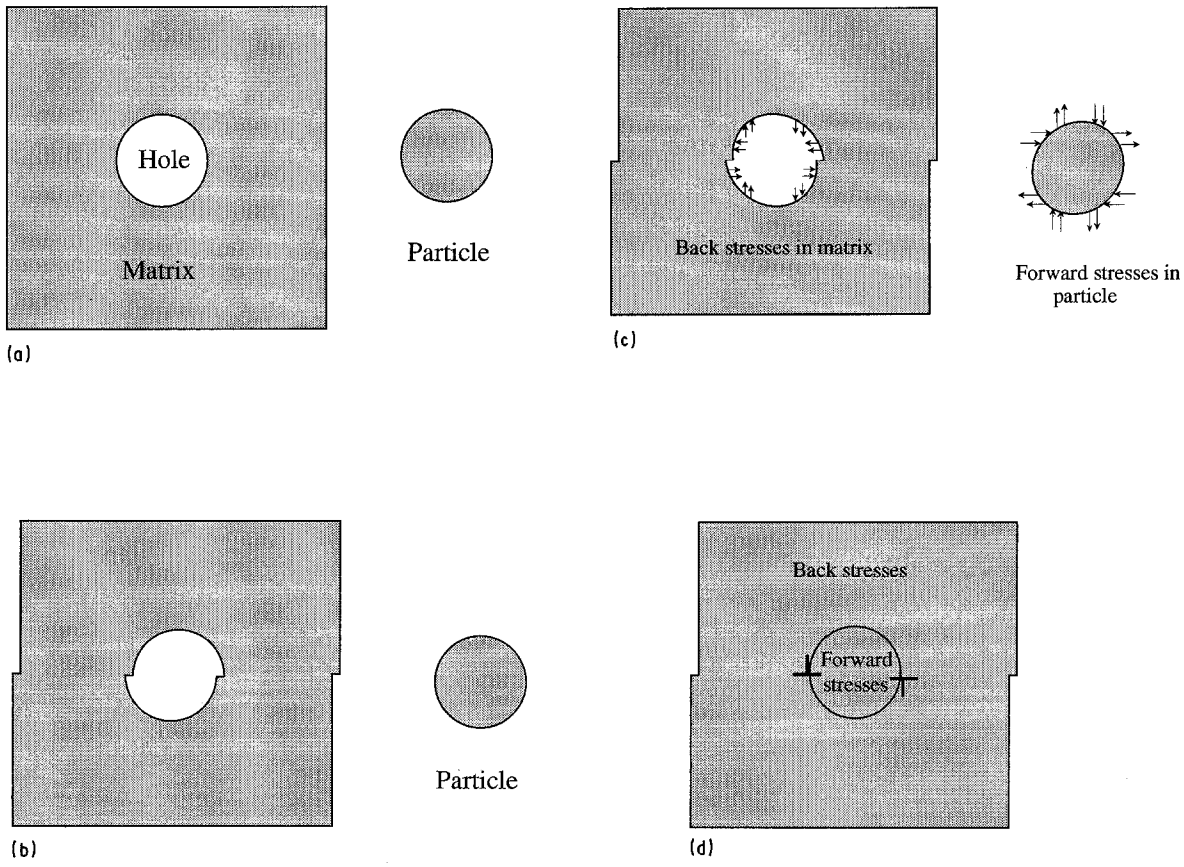

Figure 1 (a–d) Schematic representation of the origins of the internal stress in precipitation hardened alloys. (a) Removal of particle from matrix, (b) plastic deformation of matrix, (c) deformation of hole and particle until they fit, (d) Replacement of particle and formation of Orowan loop.

is impenetrable to dislocations, these only sample the internal stresses in the matrix which oppose the applied stress.

The average internal stress can be estimated by averaging the sum of the internal stresses inside and outside the particle and setting this to zero. If the plastic shear of the matrix had been homogeneous and of amount ε, then the shear stress inside the spherical particle, τ_p, would be uniform and equal to

$$\tau_p = 2\gamma\mu\varepsilon \quad (2)$$

where μ is the shear modulus and γ is a numerical constant $\approx 1/2$ [13].

The *average* internal shear stress, τ_1, in the *matrix* which is required to make the overall average equal to zero is of opposite sign, and is given by

$$\tau_i = 2(V_p/V_T)\gamma\mu\varepsilon \quad (3)$$

where V_p and V_T are the particle and the total volumes, respectively. It should be noted that τ_i tends to zero in an infinite body ($V_T \rightarrow \infty$) and hence τ_i is associated with the stresses necessary to satisfy the boundary conditions in a finite body and is not part of the normal infinite body solution for the stress field of an Orowan loop. It is therefore often called an image stress. The plastic strain, ε, can be approximated by nb/d where d is the particle diameter, b the magnitude of the Burgers vector and n the number of Orowan loops. If there is a volume fraction, f, of particles having n Orowan loops present, each will contribute a term of the form of Equation 3 and these will add to give a quasi-uniform internal shear stress

$$\tau_i = 2f\gamma\mu nb/d \quad (4)$$

using a Taylor factor of 3 and setting γ equal to 1/2, the tensile internal stress, σ_i, in the matrix is

$$\sigma_i = 3f\mu nb/d \quad (5)$$

It is this equation that will be used to calculate the internal stress resulting from measurements of the number of γ' particles which have Orowan loops in the present alloy.

It should be noted, however, that it is only loops with an Orowan character, (i.e. with Burgers vector parallel to the plane of the loop) which give rise to internal stresses as described above. Prismatic loops, having a Burgers vector perpendicular to the loop plane, do not give rise to internal stresses of the kind considered here. In fact an Orowan loop may degenerate into a number of prismatic loops by prismatic punching which releases the high strain energy inside the looped particle and at the same time removes the internal stress in the matrix [13]. At high temperatures an "unpinned" Orowan loop could rotate by climb into a prismatic configuration giving the same result. This is effectively a transfer of matter around the particle/matrix interface, changing the shape of the hole and thus relaxing the high stresses inside the particle and hence τ_i outside the particle.

It is hence clearly important to be certain that any loops counted are truly Orowan loops, not prismatic loops or loops of some other character. It will be necessary therefore to determine both the Burgers vectors and habit planes of the observed loops.

4. Experimental methods

4.1. Materials

The material used for this study was commercial Nimonic 91. The composition was Cr 28.18, Co 19.4, Ti 2.37, Al 1.5, Fe 0.9, Si 0.29, Mo 0.24, Mn 0.17, Cu 0.15, S 0.004 (mass %). The balance was nickel. The alloy was solution treated by water quenching from 1423 K after soaking for 6 h. Creep specimens were aged for 16 h at 1123 K, which produced a volume fraction of 16%, near spherical γ' particles with a mean diameter of 40 nm. Ageing increased the hardness of the alloy from 173 VPN to 367 VPN. Young's modulus was measured and found to be 225 GN m^{-2} at room temperature and 158 GN m^{-2} at 1123 K.

4.2. Creep testing

Cylindrical creep specimens with threaded ends and a 25.4 mm gauge length were machine ground from hot-worked bars of the alloy after solution treatment. Machined specimens were then aged in a vacuum, after de-greasing. Creep tests were carried out on Andrade–Chalmers type constant stress creep machines at 1073, 1123 and 1148 K. The temperature was controlled to better than $\pm$ 1 K and strains were measured using linear capacitance transducers capable of detecting a change in length of 120 nm. The extensometer system as a whole was capable of measuring strain to $\pm 2 \times 10^{-5}$.

4.3. Internal stress measurements

The strain transient dip test was used to determine internal stresses at 1123 K. Specimens were crept to a strain near the minimum creep rate and a stress reduction was then made. The strain/time behaviour was observed after the stress reduction. For small stress reductions incubation periods were observed followed by an increasing positive creep rate implying that the effective stress after a load reduction was still positive. If very large reductions were made a negative creep rate was observed which decreased in magnitude eventually becoming positive, possibly via an incubation period. This was taken to imply that the load reduction had made the effective stress negative. When a definite creep rate had been established the full load was re-applied. When the test had settled down to a creep rate near the original value, another reduction was made. The stress reduction required to make the creep rate first become negative was thus approached from above and below, and the internal stress was calculated by assuming that this stress reduction made the effective stress zero.

4.4. Electron microscopy

Thin films for transmission electron microscopy (TEM) were prepared from specimens crept to the minimum creep rate and then cooled under load to

room temperature. Slices 0.45 mm thick were cut from the specimen gauge length and 3 mm diameter discs trepanned from these by spark erosion. After grinding to a thickness of 0.25 mm, the central regions were electrolytically thinned using either a Metalthin single-stage twin-jet thinning unit or a Polaron twin-stage unit, using various perchloric acid–ethanol polishing solutions. Specimens were then examined in a Jeol 200CX electron microscope operating at 200 kV and/or in a Jeol 100CX electron microscope operating at 100 kV, with double tilt stages.

Foil thicknesses were determined using a convergent beam diffraction technique [14] and particle sizes and numbers where determined using centred dark-field micrographs; from these the volume fraction of γ' was determined. Burgers vector determinations of dislocation loops were made using the invisibility criterion $\boldsymbol{g} \cdot \boldsymbol{b} = 0$ where $\boldsymbol{g}$ is the reciprocal lattice vector for the diffracted beam and $\boldsymbol{b}$ is the Burgers vector of the loop [15]. The habit plane of dislocation loops was determined by tilting the specimen about a specific $\boldsymbol{g}$ vector until the loops appeared near edge on or circular. Finally, the nature of fringed loops around particles was examined using various weak-beam techniques.

5. Results

5.1. Creep data and internal stresses

The creep curves of Nimonic 91 are of conventional shape exhibiting quite large strains to fracture of 10%–20%. This enabled a good number of stress reductions to be made during a single creep test for the determination of internal stress.

A plot of log minimum creep rate versus log applied stress for the three temperatures is shown in Fig. 2. The transition from a relatively low to a very high stress sensitivity of the creep rate with increasing stress, typical of particle hardened alloys [1–9], is seen clearly at 1123 K as many tests were carried out at this temperature, the transition taking place at a stress of around 220 MN m^{-2}. At the other two temperatures the transition is not so obvious due to the lack of data points at low stresses, i.e. slow creep rates and long-term tests. However, in general, the stress exponents are all about 9.3 at high stresses and about 4 at low stresses.

The results of internal stress determinations by the strain transient dip test at 1123 K are shown in Fig. 3. Below an applied stress of about 230 MN m^{-2} the internal stress is proportional to the applied stress. The slope of the line is about 0.8 but it does not extrapolate through the origin. The rate of increase of the internal stress changes abruptly at an applied stress of 230 MN m^{-2}, becoming substantially constant and then possibly decreasing. It will be seen that this occurs at or very near to the transition stress for the data at 1123 K in Fig. 2, which is about 220 MN m^{-2}.

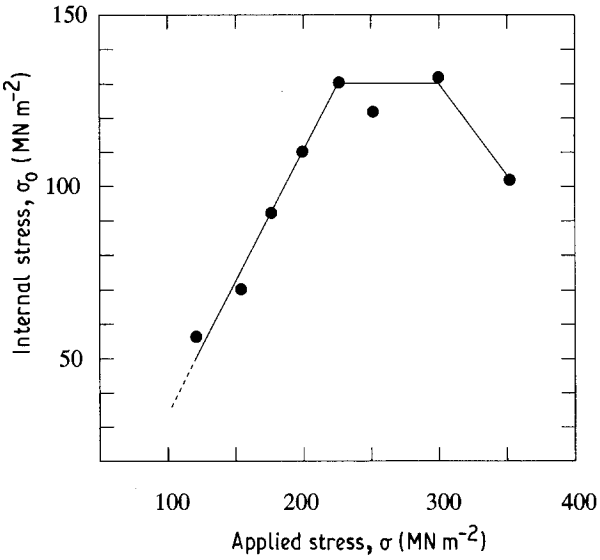

Figure 3 The relationship between the internal stress and applied stress for creep tests performed at 1123 K.

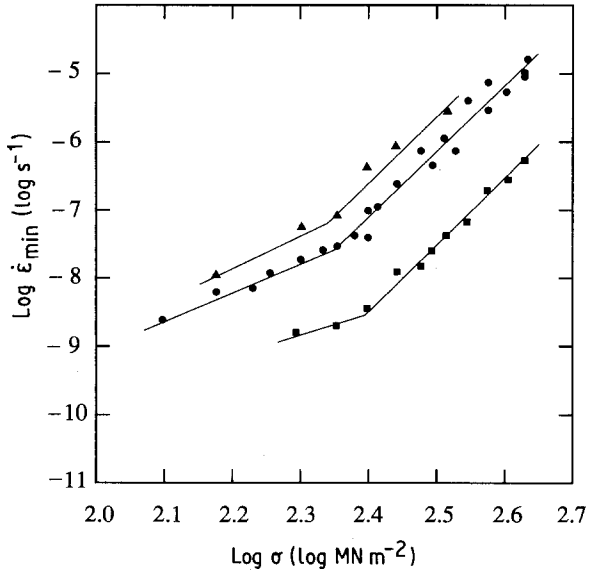

Figure 2 The minimum creep rate, ($\dot{\varepsilon}$) as a function of the applied stress, σ, at (▲) 1148 K, (●) 1123 K, (■) 1073 K.

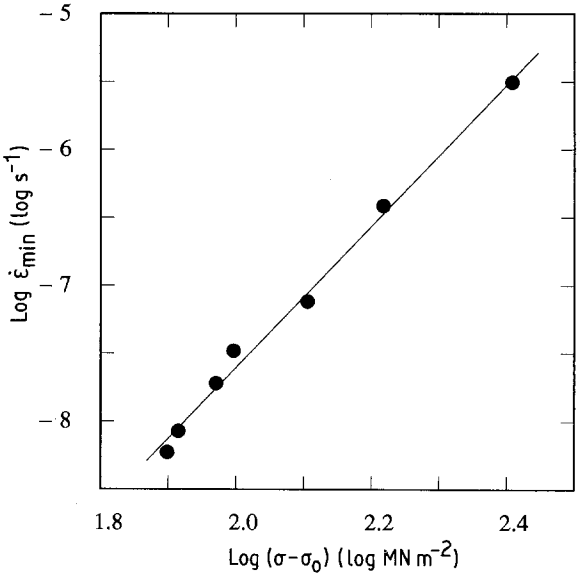

Figure 4 The minimum creep rate as a function of the effective stress.

A plot of log of the creep rate versus log of the effective stress, $\sigma_a - \sigma_i$, is shown in Fig. 4. As can be seen, there is a single line and no abrupt transition between regions of widely differing slope. The stress exponent, given by the slope of this line is 5.2.

5.2. Dislocation configurations

A large number of tests were interrupted by cooling under load at or near the minimum creep rate and the dislocation configurations examined using TEM. The configurations observed were significantly different above and below the break in the log stress, log creep rate plot (Fig. 2) but were similar in each region at all three temperatures of deformation.

At low stresses dislocations were seen bowing between γ' particles and dislocation loops were seen around particles. The loops were clearly seen in bright-field (Fig. 5) and in weak-beam (Fig. 6) imaging conditions. The partial visibility of the γ' particles arises from their coherency strain fields. Almost invariably only one loop was found to be associated with a given particle.

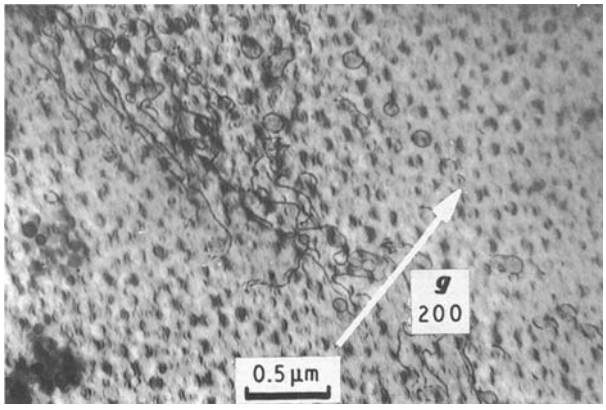

Figure 5 Electron micrograph of a specimen creep tested in the low applied stress regime ($\sigma = 150\,\mathrm{MN\,m^{-2}}$, $T = 1123\,\mathrm{K}$) showing bowing dislocations and Orowan loops imaged in bright field with $\boldsymbol{B}$ 0 0 1 and $\boldsymbol{g}$ 2 0 0.

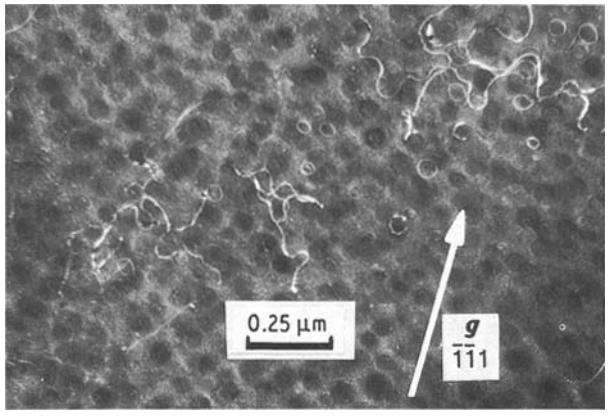

Figure 6 Electron micrograph of a specimen creep tested in the low applied stress regime ($\sigma = 225\,\mathrm{MN\,m^{-2}}$, $T = 1123\,\mathrm{K}$) showing bowing dislocations and Orowan loops imaged in weak beam with $\boldsymbol{B}$ 0 0 1 and $\boldsymbol{g}$ 2 0 0.

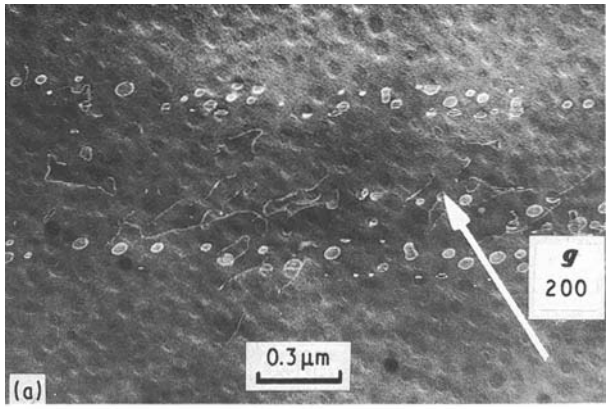

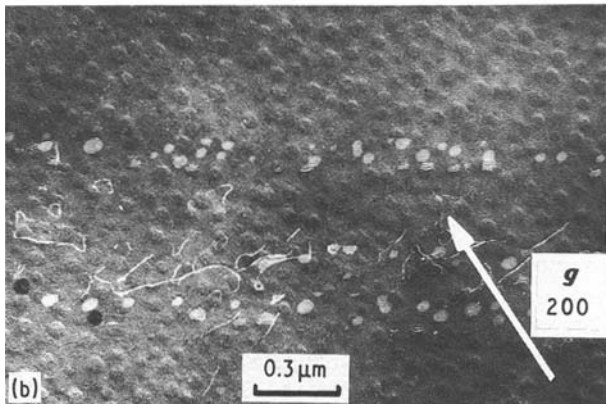

Figure 7 Electron micrographs of a specimen creep tested in the high applied stress regime ($\sigma = 325\,\mathrm{MN\,m^{-2}}$, $T = 1123\,\mathrm{K}$): (a) imaged in weak beam with $\boldsymbol{B}$ 0 0 1 and $\boldsymbol{g}$ 2 0 0. Fringed particles are visible surrounded by a distinct loop; (b) imaged in weak beam with $\boldsymbol{B}$ 0 0 1 and $\boldsymbol{g}$ $\bar{2}$ 0 0. Fringed particles are visible.

At high stresses, under bright-field conditions, an increased density of loops were seen. However, under weak-beam conditions the loops were seen to contain closely spaced fringes (Fig. 7a). Furthermore, when imaged with a reflection having a $\boldsymbol{g}$ vector of opposite sign, the loops previously visible disappeared (Fig. 7b) leaving only fringes, suggesting that they were loops of partial dislocations. The proportion of loops exhibiting fringes increased with increasing applied stress and it was occasionally possible to find a few fringed loops below the transition stresses. In general the loops were somewhat inhomogeneously distributed, usually being found in long bands, suggestive of slip-bands.

5.3. Nature of unfringed loops

In view of the discussion in Section 2 it is important to determine whether the loops observed are truly Orowan loops or have some other character. It was necessary, therefore, to determine the Burgers vector of the loops and their habit plane. It proved possibly to do this unambiguously for the unfringed loops. These are formed at all stresses but are the only loops observed in the low stress regime.

In order to determine the Burgers vector, $\boldsymbol{b}$, of the loops, the loops were imaged with a selection of two-beam diffraction vectors ($\boldsymbol{g}$ vectors) from a number of

TABLE I Value of the dot product $\boldsymbol{g}\cdot\boldsymbol{b}$ for Burgers vector determination of loops observed in a specimen crept at 150 MN m^{-2} and 1123 K

	$\boldsymbol{b}$						
$\boldsymbol{g}$	$\pm\frac{a}{2}[1\,1\,0]$	$\pm\frac{a}{2}[1\,\bar{1}\,0]$	$\pm\frac{a}{2}[1\,0\,1]$	$\pm\frac{a}{2}[\bar{1}\,0\,1]$	$\pm\frac{a}{2}[0\,1\,1]$	$\pm\frac{a}{2}[0\,1\,\bar{1}]$	Dislocation contrast
2 0 0	± 1	± 1	± 1	± 1	0	0	Visible
2 2 0	± 2	0	± 1	± 1	± 1	± 1	Visible
0 2 0	± 1	1	0	0	± 1	± 1	Invisible
1 1 $\bar{1}$	± 1	0	0	± 1	0	± 1	Visible
1 $\bar{1}$ 1	0	± 1	± 1	0	0	1	Invisible
1 $\bar{3}$ 1	1	± 2	± 1	0	1	2	Invisible

different zones (beam directions) using a foil from a specimen creep tested at 150 MN m^{-2} and 1123 K. The loops were found to be visible using $\boldsymbol{g}$ vectors of $\pm 1\,1\,\bar{1}$, 2 2 0 and 2 0 0. Thus $\boldsymbol{g}\cdot\boldsymbol{b}\neq 0$ for these $\boldsymbol{g}$ vectors. Loops were invisible when imaged using $\boldsymbol{g}$ vectors of 1 $\bar{1}$ 1, 2 0 2 and 1 $\bar{3}$ 1. Thus $\boldsymbol{g}\cdot\boldsymbol{b}=0$ for these $\boldsymbol{g}$ vectors. The scalar products of the various $\boldsymbol{g}$ vectors with appropriate Burgers vectors, $\boldsymbol{b}$, are shown in Table I, from which it can be seen that the only Burgers vector consistent with the experimental observations is $\boldsymbol{b}=\pm(a/2)\,[\bar{1}\,0\,1]$.

For the loops to be Orowan in nature, this Burgers vector has to lie in the habit plane of the loops. The habit plane of the loops can be most easily found by rotating the foil until the loops appear edge on. The diffraction pattern then allows easy identification of the habit plane [15]. A slightly less satisfactory alternative is provided if the foil can be rotated until the loops appear circular. The habit plane is then the beam direction. The latter condition is seen in Fig. 8a and b suggesting the habit plane to be (1 1 1) and the loops, having a Burgers vector parallel to $[\bar{1}\,0\,1]$, to be Orowan in character. The foil from which these micrographs were taken had a foil surface normal close to [1 2 5]. This was rotated to give a beam direction of $\boldsymbol{B}$ 1 1 2 and then rotated further to give two beam conditions. Fig. 8a is imaged with $\boldsymbol{g}$ 1 1 $\bar{1}$ and the extra rotation required to achieve this brings the beam direction closer to $\boldsymbol{B}$ 1 1 1. The loops thus appear very circular. Fig. 8b is imaged with $\boldsymbol{g}$ $\bar{1}\,\bar{1}$ 1 and the extra rotation necessary carries the beam slightly further away from $\boldsymbol{B}$ 1 1 1.

The very large tilt required to get the loops edge on was not possible with the microscope used. However, the micrograph of Fig. 9a (the same area as Fig. 8) approaches this condition. The foil was rotated to give a beam direction of $\boldsymbol{B}$ 0 0 1 and then further rotated to give a $\boldsymbol{g}$ 2 $\bar{2}$ 0 two-beam condition. This involves rotating from $\boldsymbol{B}$ 0 0 1 towards $\boldsymbol{B}$ $\bar{1}\,\bar{1}$ 2. With the beam direction exactly on $\boldsymbol{B}$ $\bar{1}\,\bar{1}$ 2 loops on the (1 1 1) plane would be edge on. The $\boldsymbol{g}$ 2 $\bar{2}$ 0 micrograph of Fig. 9a shows very elliptical loops. Furthermore the long axes of the ellipses are parallel to $\boldsymbol{g}$ 2 $\bar{2}$ 0 as expected, because this is the axis about which the foil is rotated to take the beam direction from $\boldsymbol{B}$ 1 1 1 to $\boldsymbol{B}$ $\bar{1}\,\bar{1}$ 2. Fig. 9b shows the same area but rotated to give the $\boldsymbol{g}$ 2 0 0 two-beam condition which involves rotation away from $\boldsymbol{B}$ $\bar{1}\,\bar{1}$ 2. The loops are clearly less elliptical. This confirms that the loops formed at low stresses were Orowan in character.

5.4. Nature of fringed loops

The fringes inside loops formed at high stresses are indicative of a fault of some kind on the {1 1 1} planes of the γ' phase. The spacing of fringes which arise from

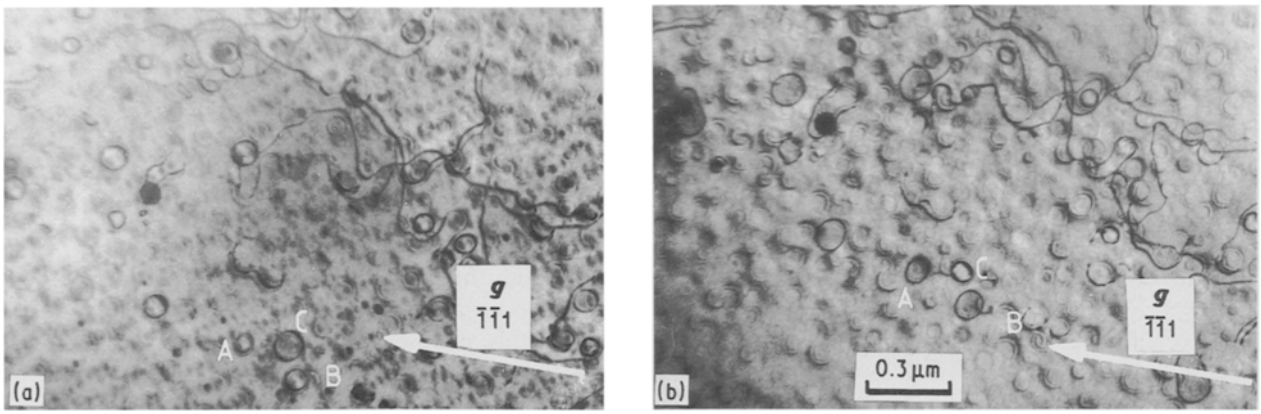

Figure 8 Electron micrographs of a specimen creep tested at 150 MN m^{-2} and 1123 K: (a) imaged in bright field with $\boldsymbol{B}$ 1 1 2 and $\boldsymbol{g}$ $\bar{1}\,\bar{1}$ 1 showing dislocation loops at A, B, C. Note that the loops are very circular; (b) imaged in bright field with $\boldsymbol{B}$ 1 1 2 and $\boldsymbol{g}$ 1 1 $\bar{1}$. Loop C has become smaller, whereas A and B have become larger.

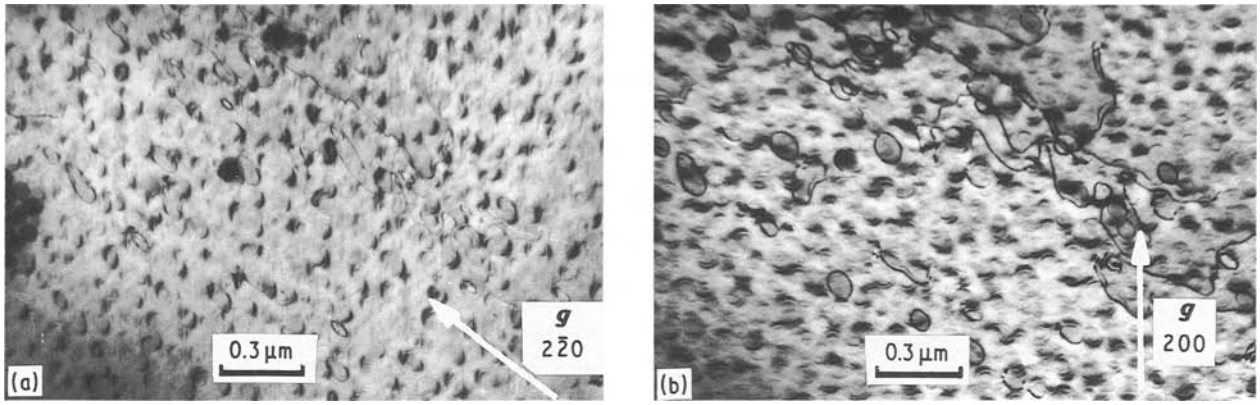

Figure 9 Electron micrographs of the same area as in Fig. 8: (a) imaged in bright field with $\boldsymbol{B}$ 0 0 1 and $\boldsymbol{g}$ 2 $\bar{2}$ 0. The dislocation loops appear almost edge on; (b) imaged in bright field with $\boldsymbol{B}$ 0 0 1 and $\boldsymbol{g}$ 2 0 0. The dislocation loops appear much less elliptical.

planar faults is inversely proportional to the deviation, s, in reciprocal space from the exact Bragg orientation, and in normal bright-field imaging the fringes would be of the order of the particle size and hence not visible. In weak-beam imaging, however, s is as much as ten times larger and it would then be possible to see fringes inside a particle as in the present case. As the γ' phase has an ordered $L1_2$ structure and is coherent with the matrix, shear of the particles by a perfect matrix dislocation would result in an anti-phase boundary on {1 1 1}. However, all attempts to image faults using a super-lattice reflection failed, suggesting that the fault is not an anti-phase boundary. It was also shown that the loops surrounding fringed particles were not perfect matrix dislocations but were partials.

There are three main types of fault on {1 1 1} in γ'. The anti-phase boundary formed by $\{1\,1\,1\}/\frac{1}{2}a\langle 1\,1\,0\rangle$ shear, as described above, has a high energy. The superlattice intrinsic stacking fault involves no violations of the nearest neighbour arrangement and hence has a lower energy. It is formed by $\{1\,1\,1\}/\frac{1}{3}a\langle 1\,1\,2\rangle$ shear. Finally there is the complex stacking fault which is formed by $\{1\,1\,1\}/\frac{1}{2}a\langle 1\,1\,2\rangle$ shear and is a combination of stacking fault and anti-phase boundary giving it a higher energy than either of the two other faults. There are also distinctions between intrinsic and extrinsic stacking faults which will not be considered here.

Based on the above information, together with the current experimental observations and previously published work concerning the interaction of dislocations with particles [16–19], a model for the formation of a faulted particle surrounded by a matrix partial dislocation can be constructed. The relation between the Burgers vectors is most easily considered in terms of the Thomson tetrahedron, one face of which is shown in Fig. 10a. The particle is first looped by a perfect matrix dislocation of Burgers vector $\boldsymbol{BA}$. This loop must penetrate a small distance into the particle, as illustrated in Fig. 10b, to form the anti-phase boundary which prevents the loop from shrinking and shearing the particle. A second lattice dislocation of Burgers vector $\boldsymbol{CA}$ then approaches the particle but is prevented from looping it by the reduction in the effective inter-particle spacing caused by the first

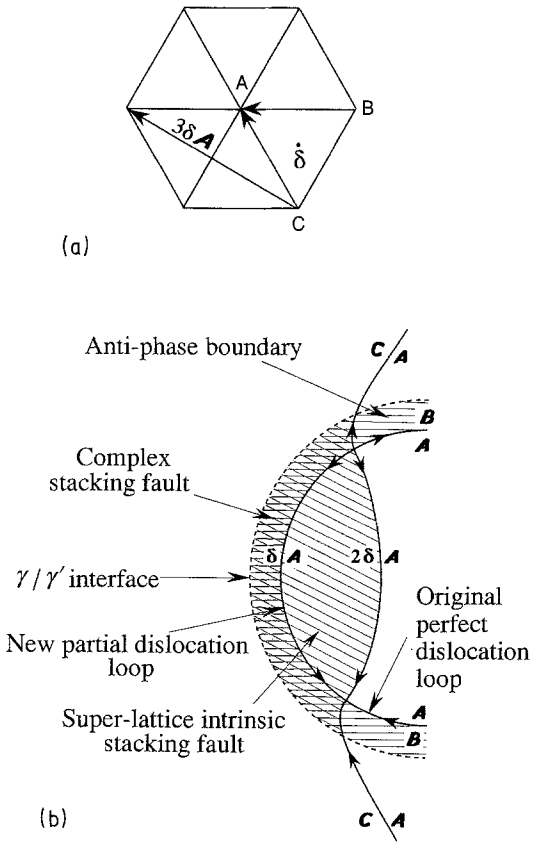

Figure 10(a) The face of a Thomson tetrahedron. The face is ABC and this has been extended to show the vector $3\delta\boldsymbol{A}$. (b) Model for the formation of fringed γ' particles.

loop. However, the two dislocations can react as follows:

$$\begin{aligned} \boldsymbol{CA} + \boldsymbol{BA} &= 3\delta\boldsymbol{A} \\ &= 2\delta\boldsymbol{A} + \delta\boldsymbol{A} \end{aligned} \qquad (6)$$

This reaction increases the energy and, if it is to occur, the applied stress must be sufficient to force the dislocations together. The dislocation with Burgers vector $2\delta\boldsymbol{A}$ forms the relatively low-energy super-lattice intrinsic stacking fault as it sweeps across the particle (Fig. 10b). If the dislocation with Burgers vector $\delta\boldsymbol{A}$ were to follow it, the fault would become a complex stacking fault of high energy. Hence it remains as a

loop around the particle held in equilibrium by the difference in surface tensions of the complex stacking fault and the superlattice stacking fault. The complete process is illustrated in Fig. 11 where, for clarity the partial penetration of the particle by the loops is not shown. In Figs 10 and 11 the sense of the Burgers vectors is given by reading the symbols from left to right looking along the arbitrarily chosen positive direction of the dislocation line.

In some cases in Nimonic 91, individual loops around more than one γ' particle were observed. In this case fringing and hence faulting can be seen to extend in between particles in the matrix (Fig. 12). This behaviour can equally be explained by the above model. It is assumed that in some regions the local inter-particle spacing is much smaller than the average spacing. In such an area the approaching ***BA*** dislocation will not be able to bow between the particles unless the stress is very high and will loop two or more particles as one, Fig. 13. The following ***CA*** dislocation

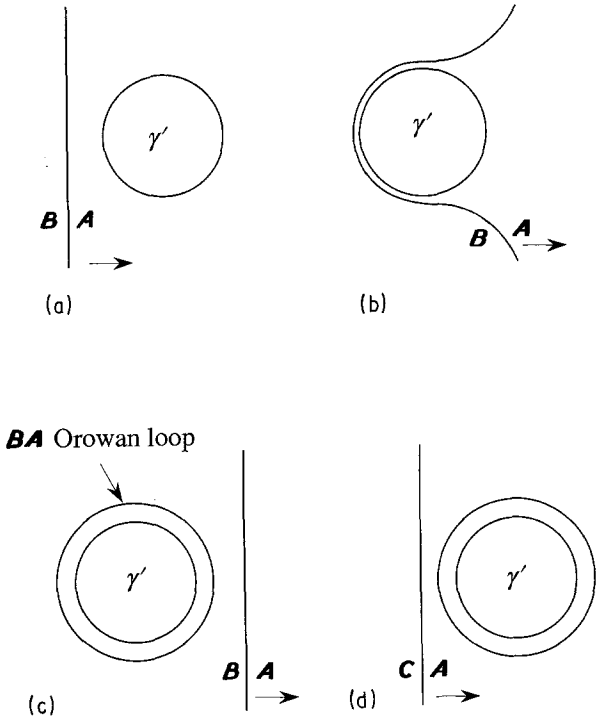

Figure 11 Schematic representation of the sequence of events involved in shearing γ' particles at high applied stresses. An Orowan loop is formed by a dislocation of Burgers vector ***BA*** (a–c). A dislocation of Burgers vector ***CA*** then reacts with the loop, shearing the particle and leaving it with a loop of partial dislocation and a super-lattice stacking fault (c–g).

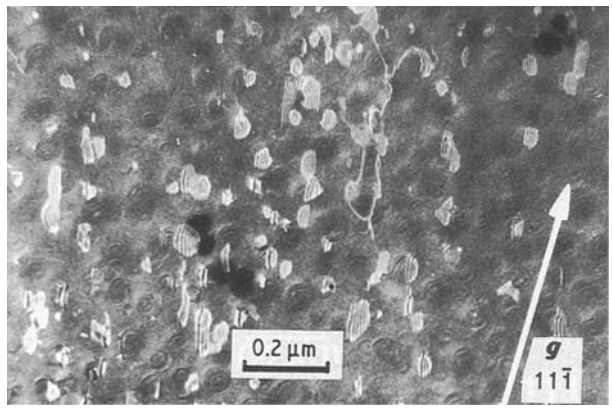

Figure 12 Weak-beam electron micrograph of a specimen creep tested at 225 MN m^{-2} and 1073 K with ***B*** 0 1 1 ***g*** 1 1 $\bar{1}$. Distinct fringing is seen within γ' particles and in the γ matrix.

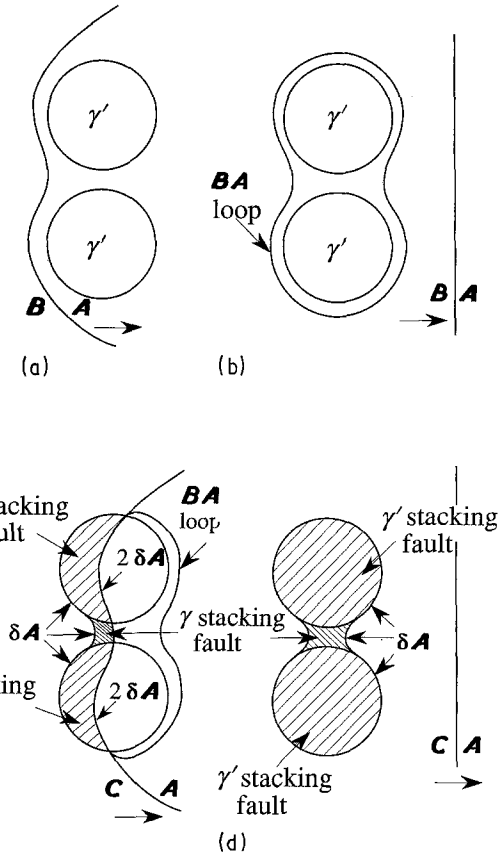

Figure 13 Schematic diagrams depicting the proposed mechanism of the partial shearing of two closely spaced γ' particles at high stresses.

then reacts as described previously resulting in a δA type partial loop residing at the γ'/γ interface and in the particles, and a matrix stacking fault between.

It is also possible that a dislocation of the same Burgers vector, BA, as the original loop around a particle could be forced sufficiently close to shear the particle in conjunction with the loop. This process would leave the sheared particle without a loop and without a fault. The reaction

$$BA + BA = 2BA \quad (7)$$

results in a greater energy increase then for Equation 6 and hence requires a larger applied stress.

On the basis of the above model it is clear that the loops around fringed particles are also Orowan in character. However, because the loops are partials, the magnitude of the Burgers vector is less than that for the loops around un-faulted particles.

6. Discussion and conclusions

It has been demonstrated that in crept specimens of Nimonic 91, Orowan loops are formed at low stresses and Orowan loops consisting of partial dislocations surrounding faulted γ' particles are formed at high stresses. It is now proposed to relate these observations to the measured values of the internal stress and to the stress dependence of the internal stress (Fig. 3). Firstly, however, it is necessary to account for the observation of these loops and their stability at the creep-testing temperatures.

The stress required to form an Orowan loop is given by [20]

$$\tau = \frac{0.4\mu b}{\pi\lambda_s(1-\nu)}\ln\left[\frac{2r_s}{b}\right] \quad (8)$$

where μ is the shear modulus, b the magnitude of the Burgers vector, λ_s the square lattice spacing, ν Poisson's ratio and r_s is proportional to the particle radius r and given by

$$r_s = \left(\frac{2}{3}\right)^{1/2} r \quad (9)$$

and the square lattice spacing λ_s is given by [21]

$$\lambda_s = \left[\left(\frac{\pi}{f}\right)^{1/2} - 2\right] r_s \quad (10)$$

with f equal to the volume fraction of particles.

Using $\mu = 59\,\mathrm{GN\,m^{-2}}$, $\nu = 0.3$, $r = 20\,\mathrm{nm}$, $b = 0.258\,\mathrm{nm}$, Equation 8 gives the Orowan shear stress as $287\,\mathrm{MN\,m^{-2}}$, i.e. a tensile stress of $574\,\mathrm{MN\,m^{-2}}$. This stress is much larger than the lowest tensile stress ($125\,\mathrm{MN\,m^{-2}}$) at which Orowan loops were observed in crept specimens of Nimonic 91. This is a general phenomenon and has been reported for many particle hardened systems deformed during creep [2, 18, 19, 22, 23] although few if any of these studies involved an unambiguous determination of the loop character. The suggestion that the theoretical value should be reduced by a factor of two if the dislocations move in pairs [20] is not convincing in this case, as dislocation pairs were never seen and the extensive use of weak-beam techniques would certainly have detected the anti-phase boundaries which result from this proposed mechanism. The main source of the discrepancy is certainly the use of the mean values of λ_s and r in Equations 8–10.

During creep, especially at low stresses, dislocations seek out paths of least resistance, avoiding regions of small particle spacing and gliding only in regions of large particle spacing, hence sampling only the tail of the particle size distribution. It is this mean value of the spacing, λ, sampled by dislocations, which should be used in Equation 8 rather than λ_s, and would result in a much lower estimate of the effective Orowan stress.

While the existence of Orowan loops at such low applied stresses can be explained qualitatively, their stability against climb at these temperatures is initially a puzzle. The driving forces for the climb processes which could convert Orowan loops to prismatic loops are high but large numbers are seen even in long-term creep tests. An explanation for this stability probably lies in the fact that the loops must partially penetrate the particle to find a stable equilibrium. This penetration must occur otherwise the surface tension of the anti-phase boundary required to balance the line tension forces and prevent the loop collapsing would not be developed. The formation of this annular ring of anti-phase boundary, as well as preventing collapse by glide would also prevent climb, because the latter would also require the extension of the fault and would be resisted by its surface tension.

The internal stress arising from Orowan loops can be determined using Equation 5 if the volume fraction of looped particles is measured. This was done with a thin foil from a specimen crept at 1123 K and $125\,\mathrm{MN\,m^{-2}}$ until it had reached the minimum creep rate. In the foil, 582 loops and 4806 particles were counted. The diffraction conditions were such that only loops of one Burgers vector were visible and so the number was multiplied by three to account for loops not imaged. With the total volume fraction of particles equal to 0.16, the volume fraction of looped particles is 0.058 and Equation 5 gives a predicted internal stress due to loops as $\sigma_i = 26\,\mathrm{MN\,m^{-2}}$. This must be compared with the value of $55\,\mathrm{MN\,m^{-2}}$ determined by the strain transient dip test. Given the uncertainties in the measurements and in the calculations, this suggests that a major part of the measured internal stress in these alloys can be accounted for by Orowan loops.

It was not possible to measure loop densities at all creep stresses as this is a very tedious and painstaking process. However, it is possble to make qualitative comments on the observed variation of internal stress with applied stress based on the qualitative observations of loop density and character. Even given the statistical variations in particle size and spacing and the extra degree of freedom provided by climb in creep, there must be a threshold value of the applied stress below which no Orowan loops can be formed in Nimonic 91. It will be noted that the straight line in Fig. 3 extrapolates to an applied stress of $50\,\mathrm{MN\,m^{-2}}$, which can be tentatively interpreted as the lower limit

of applied stress for the formation of an Orowan loop. Thereafter an increasing number of loops can be expected as the applied stress is increased and this is in qualitative agreement with the behaviour exhibited in Fig. 3 up to an applied stress of about 225 $MN\,m^{-2}$ and with the qualitative TEM observations of loop density. Above the stress of 225 $MN\,m^{-2}$ the internal stress suddenly becomes constant and partial dislocation loops are observed in the TEM. It is suggested that at these stresses, the process in which a perfect loop is converted into a partial loop becomes possible. This partially shears the particle and partially relaxes the internal stress in both particle and matrix causing the contribution to the internal stress to drop by a factor equal to the ratio of the Burgers vectors of the two dislocation loops, i.e. $(1/3)^{1/2} = 0.57$. Hence although other loops will continue to be formed, the rate of increase of internal stress with applied stress will decrease as a result of this relaxation process. At even higher stresses the process of complete shear of the particle by a dislocation of the same Burgers vector as the original loop should become possible, causing a further drop in the rate of increase in internal stress as suggested in Fig. 4.

It can be seen that in the case of Nimonic 91 a significant part of the internal stress developed during creep can be attributed to Orowan loops around particles which are stabilized against relaxation by climb, by the fault resulting from partial penetration of the particle. This is the first time that mechanically measured internal stresses have been quantitatively related to a specific dislocation configuration developed during creep. The measured variation of internal stress with the applied creep stress can be accounted for qualitatively by the observed variation of loop density with stress at low stresses and the observed initiation of relaxation processes involving partial or complete shear of the loops at high stresses.

Acknowledgements

Dr A. G. Older thanks the Science and Engineering Research Council for the maintenance grant that enabled him to carry out this work.

References

1. K. R. WILLIAMS and B. WILSHIRE, *Met. Sci. J.* **10** (1973) 176.
2. W. J. EVANS and G. F. HARRISON, *ibid.* **10** (1976) 307.
3. J. P. DENNISON, P. D. HOLMES and B. WILSHIRE, *Mater. Sci. Engng* **33** (1978) 35.
4. S. PUROSHOTHAMAN and J. K. TIEN, *Acta Metall.* **26** (1978) 519.
5. H. BURT, J. P. DENNISON and B. WILSHIRE, *Met. Sci. J.* **13** (1979) 295.
6. M. McLEAN, *Proc. Roy. Soc.* **A373** (1980) 93.
7. R. A. STEVENS and P. E. J. FLEWITT, *Acta Metall.* **29** (1981) 867.
8. W. J. EVANS and G. F. HARRISON, *Met. Sci. J.* **13** (1979) 641.
9. C. K. L. DAVIES, A. G. OLDER and R. N. STEVENS, in "Proceedings of the 4th International Conference on the Creep and Fracture of Engineering Materials and Structures", edited by B. Wilshire and R. W. Evans (The Institute of Metals, London, 1990), p. 97–107.
10. G. N. AHLQUIST and W. D. NIX, *Scripta Metall.* **3** (1969) 679.
11. D. SIDEY and B. WILSHIRE, *Met. Sci. J.* **3** (1969) 56.
12. M. F. ASHBY, *Phil. Mag.* **21** (1970) 399.
13. L. M. BROWN and W. M. STOBBS, *ibid.* **23** (1971) 1185.
14. P. M. KELLY, A. JOSTONS, R. G. BLAKE and J. G. NAPIER, *Phys. Status Solidi* **31** (1975) 771.
15. J. W. EDINGTON, "Electron Diffraction in the Electron Microscope", Vol. 2 (MacMillan, London, 1972) p. 76.
16. J. P. HIRTH, *J. Appl. Phys.* **32** (1961) 700.
17. B. H. KEAR, G. F. GIAMEI, G. R. LEVERANT and J. M. OBLAK, *Script Metall.* **3** (1969) 455.
18. A. GUIMIER and J. L. STRUDEL, in "2nd International Conference on the Strength of Metals and Alloys' (American Society for Metals, Metals Park, Ohio, 1970) p. 1145.
19. B. H. KEAR and J. M. OBLAK, *J. Phys. Coll. C7* **35** (1974) 7.
20. L. M. BROWN and R. K. HAM, in "Strengthening Mechanisms in Crystals", edited by A. Kelly and R. B. Nicholson (Elsevier, Amsterdam, 1971) p. 9.
21. D. RAYNOR and J. M. SILCOCK, *Met. Sci. J.* **4** (1970) 121.
22. V. A. PHILLIPS, *Phil. Mag.* **16** (1967) 103.
23. *Idem, ibid.* **16** (1967) 139.

Received 18 September
and accepted 28 November 1991